THE JOURNAL OF PHYSICAL CHEMISTRY C

Article

Cite This: J. Phys. Chem. C 2018, 122, 6704−6712

pubs.acs.org/JPCC

Water Confined in Nanocapillaries: Two-Dimensional Bilayer Squarelike Ice and Associated Solid−Liquid−Solid Transition

Weiduo Zhu,[†] YinBo Zhu,[‡] Lu Wang,[†] Qiang Zhu,[§] Wen-Hui Zhao,[∥] Chongqin Zhu,[⊥] Jaeil Bai,[⊥] Jinlong Yang,[†] Lan-Feng Yuan,*[,†] HengAn Wu,*[,‡] and Xiao Cheng Zeng*[,†,⊥]

[†]Hefei National Laboratory for Physical Sciences at Microscale, Department of Chemical Physics, University of Science and Technology of China, Hefei, Anhui 230026, China

[‡]CAS Key Laboratory of Mechanical Behavior and Design of Materials, Department of Modern Mechanics, University of Science and Technology of China, Hefei, Anhui 230027, China

[§]Department of Physics, University of Nevada, Las Vegas, Nevada 89154, United States

[∥]Department of Physics, Ningbo University, Ningbo, Zhejiang 315211, China

[⊥]Department of Chemistry and Department Chemical & Biomolecular Engineering, University of Nebraska-Lincoln, Lincoln, Nebraska 68588, United States

Supporting Information

ABSTRACT: Despite recent experimental evidence of the two-dimensional (2D) square ice in graphene nanocapillaries, based on transmission electron microscopy (TEM) imaging, the AA-stacked bilayer square ice structure has not been observed in all previous classical molecular dynamics (MD) simulations nor found in recent unbiased first-principles structure searches. Herein, we report the MD simulations of 2D bilayer ice formation for water confined between two parallel hydrophobic walls (nanoslit). We find a bilayer ice whose simulated TEM imaging resembles that of bilayer squarelike ice. This bilayer ice also demonstrates dynamical stability in first-principles phonon computations. The realistic structure of this bilayer ice, however, consists of two hexagonal monolayers with the AB-stacking order, where the hexagonal rings are slightly elongated with two unequal inner angles, 107 and 146° (rather than 120°). The phase diagram of the nanoslit width versus temperature exhibits a solid−liquid−solid triple point, where the second solid phase is the well-known bilayer hexagonal ice (i.e., the bilayer ice I) with an AA-stacking order, which has been experimentally produced at ambient condition in a nanoslit of graphene and MoS_2 sheet. Such a solid−liquid−solid triple point exhibits some resemblance to that shown in the pressure−temperature phase diagram for bulk ice I−water−ice III phases.

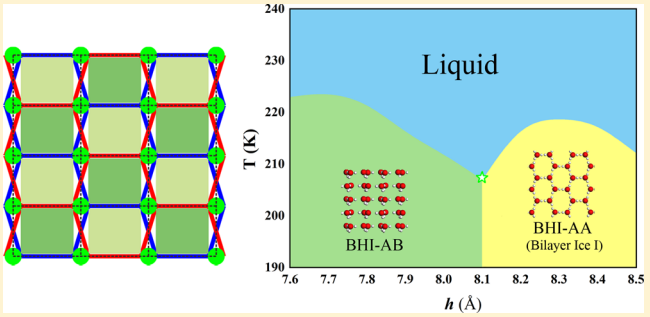

INTRODUCTION

Water is ubiquitous in nature and continues to be a subject of intense interest owing to its close relevance to biological, environmental, geological, and physical processes.[1,2] Water exhibits a variety of crystalline phases due to the extraordinary ability of water molecules to form diverse network of hydrogen bonds in response to different external pressure and temperature. The phase diagram of bulk water is rich with at least 18 bulk crystalline ice phases being realized in the laboratory and several from theoretical predictions.[3] Nanoscopic confinement adds a new physical dimension for the confined water to adapt. Depending on the length scale of the confinement, many new phases of crystalline ice can arise, as well as new phase behavior not seen in bulk phases. Indeed, numerous low-dimensional ice phases have been revealed from computer simulations. For instance, water confined in carbon nanotubes can form square, pentagonal, hexagonal, and octagonal single-walled ice nanotubes.[4−7] Under high hydrostatic pressure, one-dimensional (1D) high-density nanoice can exhibit multistranded helical structures.[8] Water confined between two parallel hydrophobic walls can form many two-dimensional (2D) monolayer ices,[9,10] including low-density hexagonal monolayer ice, mid-density flat rhombic monolayer ice (fRMI), puckered rhombic monolayer ice (pRMI), and high-density square ice,[10−18] as well as various bilayer ices with similar patterns (in top view) as the monolayer ices mentioned above,[19−23] or even new top-view patterns not seen in the monolayer ices, such as interlocked pentagonal ice,[24] square tube,[25] triangular,[16,26] and low-density and very high density amorphous ice.[20,21,27]

Experimental evidences of low-dimensional ice phases have been growing over the past decade. Jinesh and Frenken reported perhaps the first experimental evidence of 2D ice

Received: January 7, 2018
Revised: February 26, 2018
Published: February 28, 2018

DOI: 10.1021/acs.jpcc.8b00195
J. Phys. Chem. C 2018, 122, 6704−6712

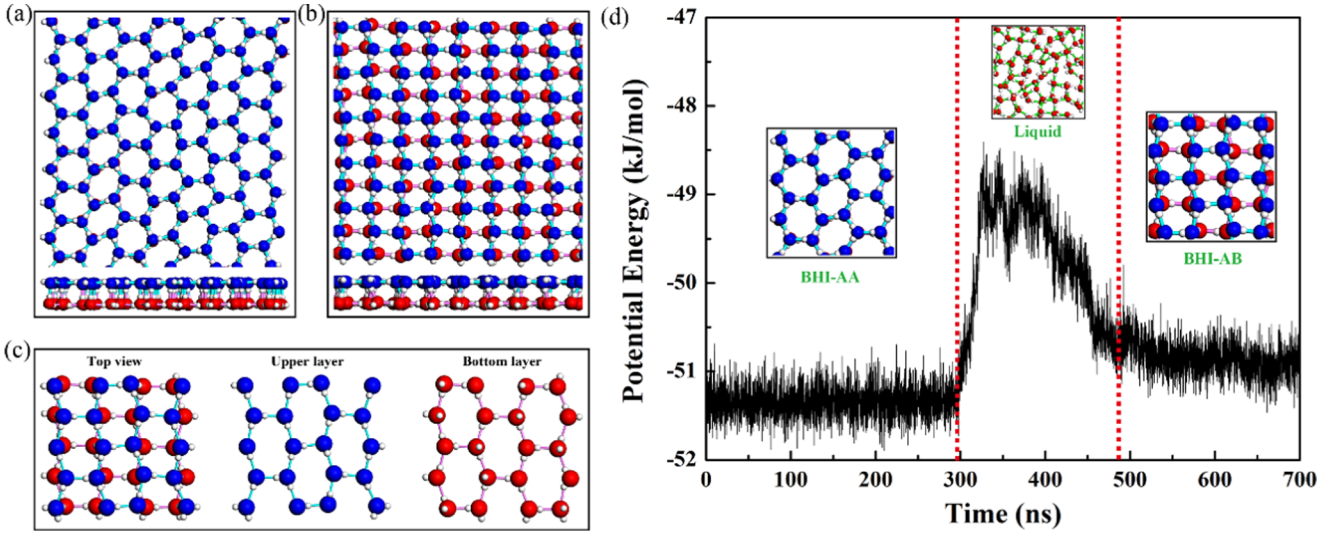

Figure 1. Inherent structures of two bilayer ice phases formed in nanoslits. (a) Top (upper) and side view (lower) of bilayer hexagonal ice with the AA-stacking order (BHI-AA; at P_L = 450 MPa, T = 200 K, and h = 8.4 Å). (b) Top and side views of the bilayer squarelike ice with the AB-stacking order of elongated hexagonal rings (BHI-AB; at P_L = 450 MPa, T = 210 K, and h = 7.7 Å). (c) Zoom-in view of the BHI-AB with upper monolayer in blue and bottom layer in red. In the top view, each pair of neighboring water molecules (in blue and red) is slightly staggered and connected by the interlayer hydrogen bond, resulting in an approximate squarelike AA-stacking pattern for the whole structure. In (a)−(c), blue, red, and white balls denote the oxygen atoms in the top layer, oxygen atoms in the bottom layer, and hydrogen atoms, respectively. The cyan and pink short lines represent the hydrogen bonds in the top and bottom layers, respectively. (d) Time-dependent potential energy (per water molecule) of the system during the MD simulation. The solid (BHI-AA)−liquid−solid (BHI-AB) transition occurs at T = 210 K, P_L = 450 MPa, and h = 7.7 Å. The insets illustrate the snapshots of the three phases of water at different time stages of MD simulation.

formation at room temperature under extreme confinement.[28] Later, a 2D bilayer hexagonal ice (BHI) formed on graphene (without the confinement) below 140 K was observed by Kimmel et al.[29] This bilayer hexagonal ice was also observed recently to form inside the nanoslit consisting of a graphene and MoS_2 sheet in ambient condition.[30] Algara-Siller et al. reported the transmission electron microscopy (TEM) imaging evidence of 2D monolayer and bilayer square ices, both predicted to form within graphene nanocapillaries at room temperature.[15] The 2D square ice is known to have a high packing density with a lattice constant of ∼2.83 Å. The 2D monolayer squarelike ices, such as the fRMI and pRMI, have already been reported in previous molecular dynamics (MD) simulations.[9−11,16] However, to date, the bilayer square ice with the AA-stacking pattern (top view) has not been observed in MD simulations, including several more recent ones aiming at confirming the TEM experiment.[31−35] Although Mario et al. indicated that the AA-stacking bilayer ice identified in the TEM experiment is consistent with their minimum-energy structure of bilayer ice on the basis of the ReaxFF force field,[35] the bilayer square ice was found unstable with respect to the high-density phases based on density functional theory (DFT) computation.[36] The difference between the TEM experiment and theoretical predictions has been a subject of inquiry on the existence of bilayer square ice within the nanocapillary or nanoslit. Clearly, more studies are needed to resolve the difference.

In this work, we attempt to identify the bilayer ice structure whose simulated TEM image can look like the TEM image taken by Algara-Siller et al.[15] On the basis of comprehensive MD simulations with TIP4P/2005 water model, we identify a bilayer ice whose simulated TEM image exhibits a squarelike pattern, or more precisely, a rectangle pattern. The realistic structure of this bilayer squarelike ice is the AB-stacking order of two hexagonal monolayer ices, each exhibiting an elongated hexagonal ring structure. The two bilayer hexagonal ices (BHIs) with AA- and AB-stacking orders can be transformed either directly from one another or indirectly through a liquid phase, via changing the width of the slit pore.

RESULTS AND DISCUSSION

In the first series of MD simulations with P_L = 450 MPa, the formations of two different bilayer ices were observed, one being the bilayer hexagonal ice with AA-stacking (BHI-AA) at 200 K and h = 8.4 Å (wider slit) and another being BHI-AB at 210 K and h = 7.7 Å (narrower slit). Here, the AA-stacking means that the positions of hexagonal rings in the upper layer overlap with those in the lower layer in the surface normal z-direction, whereas the AB-stacking means that the positions of elongated hexagonal rings in the upper layer do not overlap with those in the lower layer in the z-direction, but staggered with the half length of hexagonal unit. Figure 1 displays the inherent structures of both BHIs, obtained by applying the steepest-descent method to the final configuration of the system.[27] More specifically, BHI-AA (Figure 1a) is obtained via gradually cooling the bilayer water in a nanoslit of h = 8.4 Å, as done in previous studies.[27,37] Note that a recent experiment has confirmed the formation of the BHI-AA in hydrophobic nanoslit at room temperature.[30] More interestingly, BHI-AB (Figure 1b and Movie S1) exhibits a top-view pattern that resembles a bilayer squarelike ice in the AA-stacking order. However, as illustrated in Figure 1c, BHI-AB actually consists of two AB-stacked hexagonal monolayers, each exhibiting elongated hexagonal rings. Although the bilayer structures with elongated hexagonal rings have been reported in previous studies,[34,38] the crystalline phase like BHI-AB and related phase behavior have not been studied.

BHI-AB satisfies the ice rule in that every water molecule is a double donor and a double acceptor of hydrogen bonds to its four neighbor molecules. The interlayer molecular interaction

DOI: 10.1021/acs.jpcc.8b00195
J. Phys. Chem. C 2018, 122, 6704−6712

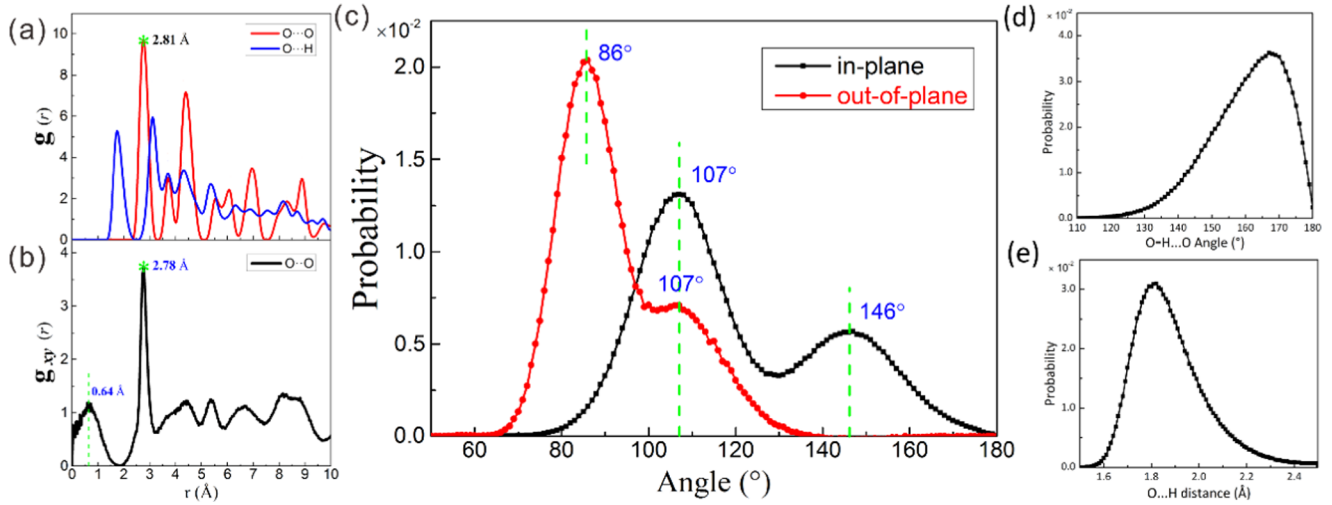

Figure 2. Structural characteristics of BHI-AB from MD simulations. (a) The oxygen−oxygen and oxygen−hydrogen radial distribution functions; namely, O−O RDF and O−H RDF, respectively. The green point denotes the first sharp peak in the O−O RDF with the location of ∼2.81 Å. (b) Lateral oxygen−oxygen radial distribution function (lateral O−O RDF). The green dashed line denotes the first low peak with the location of ∼0.64 Å, demonstrating the staggered offset of oxygen atoms in the AB-stacked elongated hexagonal rings. The green point denotes the sharp peak in lateral O−O RDF with the location of ∼2.78 Å. (c) The in-plane and out-of-plane O···O···O angle distributions in the whole structure of BHI-AB. The green dashed lines marked with angle values denote the characteristic angles. (d) The O−H···O angle distribution for the BHI-AB. (e) The O···H distance distribution for the BHI-AB. All of the statistics are from the MD snapshots within a sampling time of 10 ns.

in BHI-AB is relatively strong because the two layers are connected via hydrogen bonds between every pair of two opposing water molecules (side view in Figure 1b). In all the snapshots within the last 40 ns sampling time of the MD equilibrium run (Figure S1), each pair of two opposing water molecules in the two layers forms an approximate AA-stacking configuration in the top view; therefore, a squarelike pattern of the whole structure can be seen in the top view after taking the time-averaging effect into account.

In another series of MD simulations, we found that BHI-AB can be achieved from BHI-AA via slowly reducing the width h of the slit pore. (Figure 1d and Movie S2). Note that this BHI-AA to BHI-AB transformation could show the Oswald staging phenomenon. Here, the Oswald staging refers to the phase behavior such that an intermediate liquid state arises during the solid−solid transformation, at a given h of 7.7 Å, exhibiting a solid−liquid−solid transformation behavior during the MD simulation. In the middle stage of the simulation, the recorded diffusion constant of water increases up to 2×10^{-7} cm^2/s and keeps this value for about 70 ns, followed by a gradual decrease toward a value for typical solid phase. Meanwhile, as shown in Figure 1d, the time-dependent potential energy (per molecule) also reflects the Oswald staging behavior, where the liquid has the highest potential energy, whereas the BHI-AA has the lowest potential energy. The Oswald staging phenomenon was previously observed in the transition from BHI-AA to bilayer very high density amorphous (BL-VHDA2).[21]

To gain more insight into the structural features of BHI-AB, we computed the density profiles in the z-direction (Figure S2) and radial distribution functions (RDFs) (Figure 2a,b). As can be seen from the oxygen density distribution in Figure S2, BHI-AB is a flat bilayer ice in which the oxygen atoms in each layer are in the same plane. The ratio of the intralayer hydrogen atoms and the interlayer hydrogen atoms is about 3:1, indicating that on average, for each pair of two opposing water molecules in the two layers, an inerratic hydrogen bond is formed between a hydrogen atom in one layer and an oxygen atom in the opposing layer. These interstratified hydrogen bonds are likely the primary reason for the high stability of this AB-stacked structure, which can be seen as near-AA-stacking of the oxygen atoms in a wide range of temperatures and lateral pressures. The oxygen−oxygen RDF in Figure 2a illustrates the first sharp peak in $g_{O-O}(r)$, located at ∼2.81 Å, which corresponds to the first neighboring distance between the oxygen atoms in BHI-AB. The well-separated peaks and valleys indicate that BHI-AB has a long-range crystalline order. As shown in Figure 2b, the oxygen−oxygen lateral RDF $[g_{xy}(r)]$ also exhibits a sharp peak at ∼2.78 Å, which is very close to the measured value in the experiments.[15] Moreover, $g_{xy}(r)$ has a small peak located at ∼0.64 Å, indicating the staggered offset of the oxygen atoms in the AB-stacked elongated hexagonal rings. In Figure 2c, the in-plane and out-of-plane O···O···O angle distributions in snapshots of BHI-AB are computed in the MD simulations within 100 ns equilibrium run. For the in-plane angle distribution (black line with square symbols), the two peaks are located at 107 and 146°, with the ratio of the two corresponding peak values being 2:1. The two angles correspond to the two inner angles of elongated hexagonal ring in BHI-AB. In the formation of BHI-AB (Figure 1 and Movie S1), the hexagonal network is squeezed under a relatively higher lateral pressure,[39] resulting in two smaller angles (∼107°) and one larger angle (∼146°) compared to that (120°) for a perfect hexagonal network.

For BHI-AA, it is known that the interlayer hydrogen bonds are perpendicular to the plane of each monolayer due to the strict AA-stacking order. What about the interlayer hydrogen bonds for BHI-AB? The out-of-plane (interlayer) angle distribution in Figure 2c (red line with circle symbols) demonstrates that the first peak is located at about 86° with a shoulder being located at about 107°, indicating that the interlayer hydrogen bonds are not perpendicular to the plane of each monolayer. This feature is consistent with the interlayer distance of BHI-AB being smaller than that of BHI-AA, as the AB-stacking order for the two monolayers allows a small offset of oxygen atoms in the two monolayers as seen from the top view. In Figures 1b and 2b, it is clear that each pair of water

DOI: 10.1021/acs.jpcc.8b00195
J. Phys. Chem. C 2018, 122, 6704−6712

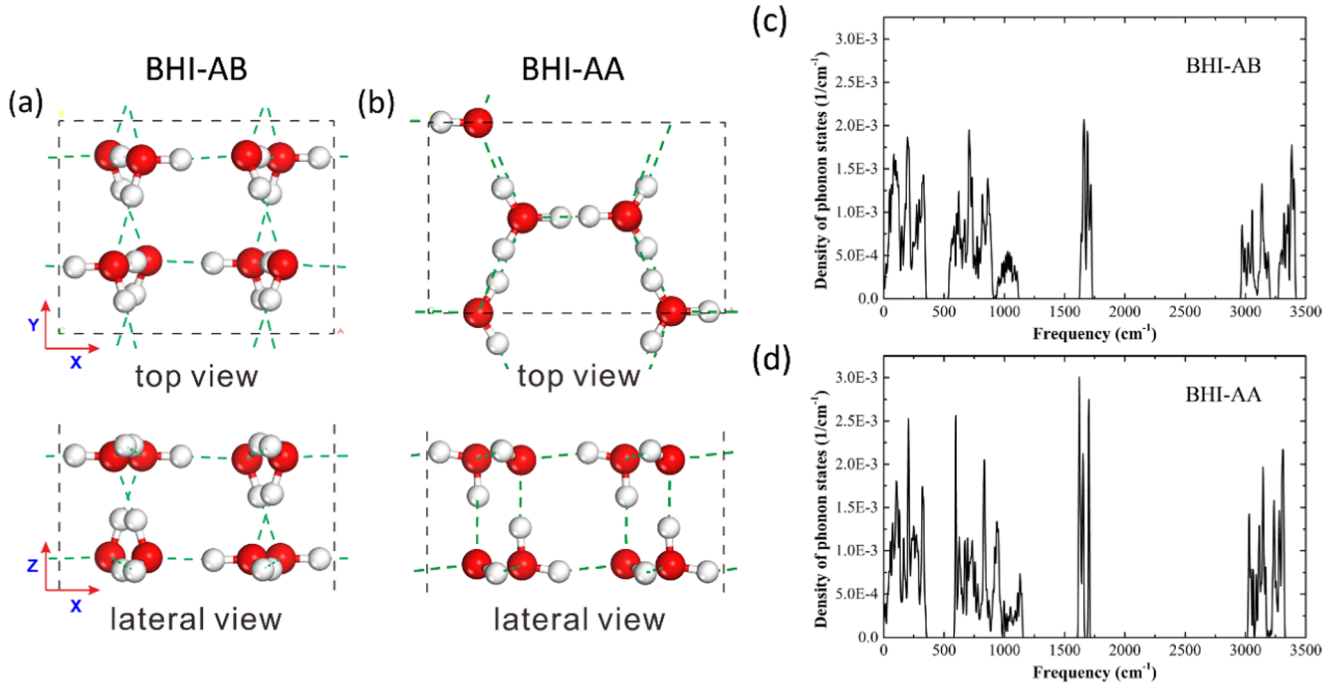

Figure 3. Unit cells of BHI-AB and BHI-AA optimized using a DFT method (upper panel: top view; lower panel: side view). (a) BHI-AB (L_x = 7.04 Å and L_y = 5.45 Å) and (b) BHI-AA (L_x = 7.85 Å and L_y = 5.04 Å). L_x and L_y are the lattice constants. The black dashed lines illustrate the boundaries of unit cell. The red and white balls represent the oxygen and hydrogen atoms, and the olive dashed short lines denote the hydrogen bonds among water molecules. (c, d) Computed phonon density of states of BHI-AB and BHI-AA bilayer ice using the DFPT method implemented in Materials Studio 7.0 package, respectively.

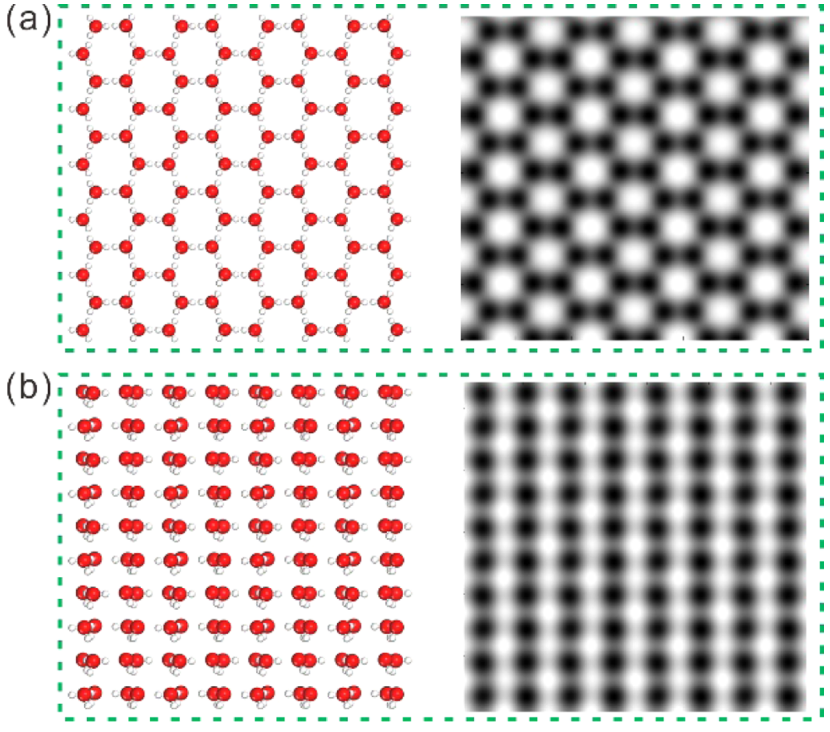

Figure 4. Simulated transmission electron microscopy (TEM) images of two bilayer ice structures: (a) BHI-AA (left panel: atomic structure; right panel: simulated image) and (b) BHI-AB. Another simulated TEM image of the larger-scale BHI-AB is illustrated in Figure S4 in the Supporting Information.

molecules in opposing layers are staggered with a small offset. We also analyzed the distribution of the O−H···O angles and the O···H distances of the hydrogen bonds in the BHI-AB snapshots (Figure 2d,e). The O−H···O angle is not far from 180°, suggesting the validity of the localized orbital picture of an O−H bond being approaching to a lone pair. Although a larger distortion can decrease the depth of the potential well, for angles less than 140° there is an onset of a significant loss of

DOI: 10.1021/acs.jpcc.8b00195
J. Phys. Chem. C 2018, 122, 6704−6712

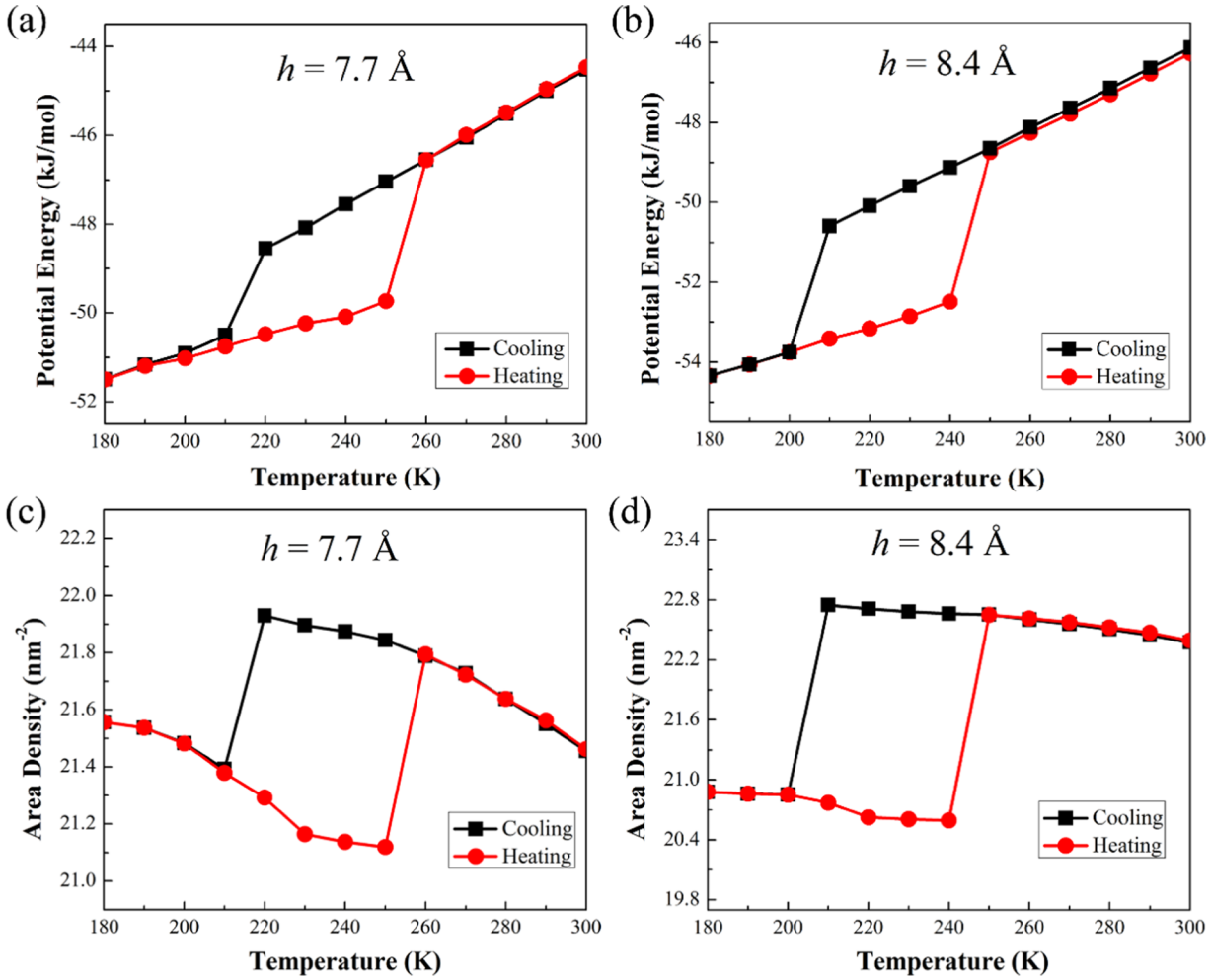

Figure 5. (a, b) Potential energy (per water molecule) versus temperature in the cooling process and heating process, respectively. (a) BHI-AB at h = 7.7 Å. (b) BHI-AA at h = 8.4 Å. (c, d) The area density versus temperature for (c) BHI-AB and (d) BHI-AA in the cooling and heating process, respectively.

energy.[40] This means that the distortion of about 167° for BHI-AB is quite reasonable. As Figure 2e shows, the peak value is about 1.82 Å, close to the O···H distance (1.79 Å) of Pauling's representation of ice.[41]

To examine the dynamic stability of BHI-AB, we performed the density functional theory (DFT) calculations using the CASTEP[42] program implemented in the Materials Studio 7.0 package. The optimized structures of BHI-AB and BHI-AA, based on the Perdew–Burke–Ernzerhof (PBE)[43] exchange-correlation functional, are presented in Figure 3a,b. The computed cohesive energies are −0.62 and −0.54 eV per water molecule for the BHI-AA and BHI-AB, respectively. The phonon spectra (Figure 3c,d) are computed by using the density functional perturbation theory (DFPT),[44] as implemented in CASTEP. No imaginary frequency is found within the entire Brillouin zone, also confirming the dynamic stability of both bilayer ices. We also optimized both structures based on PBE-D[45] exchange-correlation functional and computed the phonon spectra (Figure S3). The results are consistent with the PBE computation, confirming the dynamic stability of both bilayer ices. From the phonon spectra, one can also assign peaks for OH-bending (around 1760 cm^{-1}) and OH-stretching (around 3400 cm^{-1}), as well as low-frequency collective motion regions.

Figure 4 displays the simulated TEM images of both BHI-AA and BHI-AB structures, based on the DFT optimized structures and using the QSTEM software.[46] The simulated TEM parameters are set to mimic the experimental conditions (accelerating voltage and spherical aberration coefficient).[15] High-contrast dark spots correspond to oxygen and reflect near-center of the mass positions of the water molecules. The hydrogen atoms cannot be visualized by TEM. As shown in Figure 4a, the simulated TEM image of BHI-AA exhibits a hexagonal pattern, similar to the TEM image viewed from the [0001] zone axis of ice I_h.[47] In contrast, the simulated TEM image of BHI-AB (Figures 4b and S4) exhibits a squarelike pattern apparently, resembling to, to some extent, but not the same as the experimental TEM pattern reported[15] (see Figure 2 in ref 15). A closer look at the simulated pattern shown in Figure 4b indicates that the simulated TEM pattern is a rectangle pattern whose "lattice constants" are L_x = 7.04 Å and L_y = 5.45 Å. Without knowing the original crystalline structure of the bilayer ice, the simulated TEM image of BHI-AB could be viewed as stemming from a bilayer squarelike or rectangle ice with the AA-stacking. Unlike that of the monolayer ices, the TEM image alone cannot determine the realistic atomic structure of a bilayer ice, only the projected pattern of oxygen atoms in the normal direction.

DOI: 10.1021/acs.jpcc.8b00195
J. Phys. Chem. C 2018, 122, 6704−6712

To shed light on the phase transitions of BHI-AB and BHI-AA, the MD simulations of heating and cooling processes at different fixed nanoslit width h were carried out. The rapid changes in potential energy (per water molecule) and associated obvious hysteresis loops, as shown in Figure 5, indicate that the phase transition between bilayer liquid water and corresponding solid phase is a strong first-order.[27,48,49] In a relatively narrower slit of h = 7.7 Å (Figure 5a), the bilayer liquid water freezes into the BHI-AB at T = 210 K with a sharp change in the potential energy of 2.0 kJ/mol. In the inverse process of heating, BHI-AB transforms into a liquid state at T = 260 K, indicating that BHI-AB can be metastable at a relatively high temperature (superheating). The cooling/heating processes between liquid water and BHI-AA in wider slits (8.1 Å < h < 8.5 Å) display similar changes in potential energy. In Figure 5b, the apparent melting temperature of BHI-AA is about 250 K, which is not as high as observed in previous work.[48] The difference is mainly due to the lateral pressure, which is much higher here than that used in previous work. Meanwhile, an abrupt change in the area density in the cooling/heating process of both structures can be also seen in Figure 5c,d. The area density of BHI-AB is slightly higher than that of BHI-AA, indicating that the hexagon rings in BHI-AB are squashed. Nevertheless, the area density of BHI-AB is still lower than that of bilayer square ice, which is why its TEM pattern is rectangular rather than square.

We have also performed extensive MD simulations to derive the temperature versus nanoslit width (T−h) phase diagram that includes BHI-AA and BHI-AB phases for a given lateral pressure of P_L = 450 MPa. This phase diagram plotted in Figure 6 can give an intuitive perspective for the two bilayer solid phases and a bilayer liquid water. The solid−liquid phase boundaries are determined by using the two-phase coexistence simulation method. As illustrated in Figure 6, the boundaries between the liquid and solid phases are plotted by connecting the transition temperature points at several given h. A triple point (marked as a green star) for the three-phase coexistence (BHI-AB/liquid/BHI-AA) is located within the region of 8.0 Å < h < 8.2 Å and of temperature 205 K < T < 210 K. Such a solid−liquid−solid triple point exhibits some resemblance to that shown in the pressure−temperature phase diagram for the bulk ice I−water−ice III phases. It is clear that BHI-AB can be stable at higher temperatures (>220 K) near h ∼ 7.7 Å. When the temperature is between 205 K (triple point) and 220 K, there exists a liquid region between the BHI-AB and BHI-AA phases, corresponding to the solid−liquid−solid transition shown in Figure 1d.

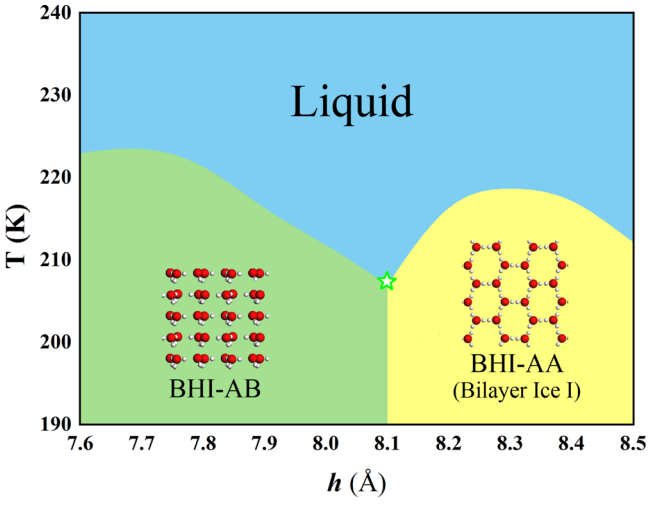

Figure 6. A phase diagram of BHI-AB and BHI-AA in the T−h plane for P_L = 450 MPa. The open star is the triple point, estimated to be located between 205−210 K and 8.0−8.2 Å. Two solid phases have different symmetries and are thus separated by a phase boundary. The insets illustrate the structures of BHI-AB and BHI-AA, respectively. Each liquid−solid phase boundary exhibits a local maximum.

As reported in previous studies,[15,50] the phase boundary for the liquid−solid phase transition for low-dimensional ice is typically convex upward and intersects with the nearby solid−solid boundary. The liquid−solid phase boundaries shown in Figure 6 can be further analyzed by using the Clapeyron equation for confined system[22,51]

$$\left(\frac{\partial T}{\partial h}\right)_{P_L} = -\frac{(a\Delta P)^{\alpha} - (a\Delta P)^{\beta}}{s^{\alpha} - s^{\beta}} = -\frac{f^{\alpha} - f^{\beta}}{s^{\alpha} - s^{\beta}}$$

where $f = a\Delta P$ is the average force on the hydrophobic wall (a is the wall area and ΔP is the pressure difference between the normal and lateral directions)[22] and s denote the entropy. The superscripts α and β denote two different phases of water molecules, confined between two hydrophobic surfaces.[51] Let α and β represent the liquid phase and an ice phase, respectively, so that $s^{\alpha} - s^{\beta} > 0$. Hence, $\partial T/\partial h$ is dependent on the free-energy difference $f^{\alpha} - f^{\beta}$. When the nanoslit width h is less than an optimal value for the ice, f^{β} is positive and larger than $|f^{\alpha}|$, that is, $f^{\alpha} - f^{\beta} < 0$, then $\partial T/\partial h > 0$. In contrast, when h is larger than the optimal value, that is, $f^{\beta} < 0$ and $f^{\alpha} - f^{\beta} > 0$, then $\partial T/\partial h < 0$. At the optimal value, $f^{\alpha} - f^{\beta} = 0$ and $\partial T/\partial h = 0$, the liquid−solid phase boundary would exhibit a local maximum.[51]

Moreover, we also found an interesting phase transition from BHI-AB to the high-density bilayer square-tube ice (also named as bilayer very high density ice (BL-VHDI)[21]) via direct lateral compressing BHI-AB. As illustrated in Figure 7a, the abrupt increase in area density indicates a first-order phase transition from BHI-AB to BL-VHDI when the lateral pressure is >1.0 GPa. In BL-VHDI, the water molecules of each layer exhibit rhombic arrays with a slight dislocation (Figure S5a). As shown in Figure S5b, the simulated TEM image of BL-VHDI exhibits a pattern consisting of both squares and rhombus. Figure 7b shows that the transition from BHI-AB to BL-VHDI also exhibits the Oswald staging phenomenon, namely, an unstable intermediate liquid state arises during the solid−solid transition. In the middle stage of the simulation, the recorded diffusion constant of water increases up to 1.0 × 10^{-7} cm^2/s and is kept for about 2.5 ns. Then, the diffusion constant gradually decreases toward a much smaller value of 2.4 × 10^{-10} cm^2/s, comparable to the typical value of solid phase.

Note that the solid−liquid−solid phase transitions with the Oswald staging phenomenon are seen in the transformation among three different bilayer ices. A schematic plot that demonstrates path to inducing the phase transition among the three solid phases is shown in Figure 7c. The phase transition from BHI-AA to BHI-AB can be realized through the reduction of nanoslit width under fixed lateral pressure and temperature, whereas the phase transition from BHI-AB (or BHI-AA) to BL-VHDI can be realized through the increase in lateral pressure (lateral compression) under fixed nanoslit width and temperature. Similar transformation with arisen intermediate liquid state has also been seen in the transition from bilayer triangle ice to ABA-stacked trilayer squarelike ice.[52] In those solid−

DOI: 10.1021/acs.jpcc.8b00195
J. Phys. Chem. C 2018, 122, 6704−6712

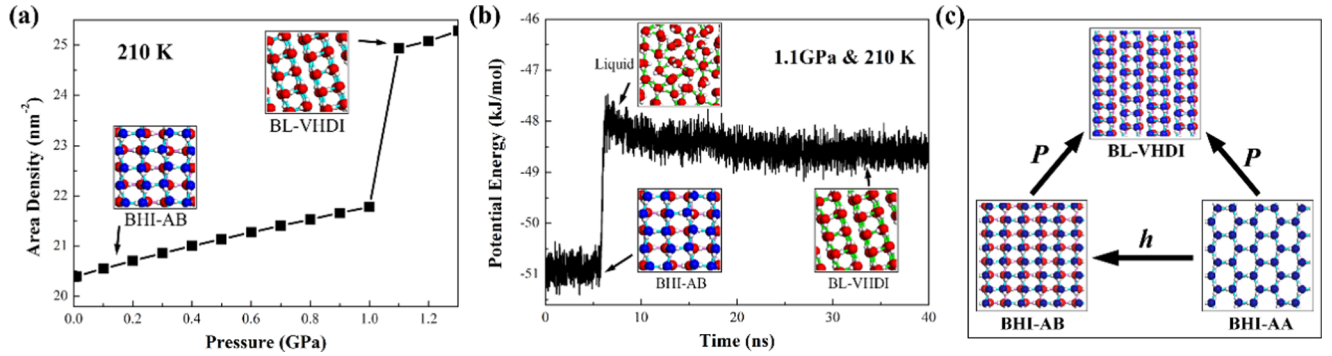

Figure 7. (a) Area density as a function of lateral pressure in the compression process at T = 210 K and h = 7.7 Å. (b) Time-dependent potential energy (per water molecule) during the MD simulation of the transformation from BHI-AB to BL-VHDI. This solid−liquid−solid transition occurs at T = 210 K, P_L = 1.1 GPa, and h = 7.7 Å. The insets illustrate the snapshots of the three phases of water at different time stages. (c) Schematic relationship of phase transition among the three ice phases. BHI-AA can transform into BHI-AB by the compression effect of nanoslit width under fixed lateral pressure (at 450 MPa) and temperature (at 210 K). BHI-AB can transform to BL-VHDI through the compression effect of lateral pressure under fixed channel width (of 7.7 Å) and temperature (at 210 K). The phase transition between BHI-AA (BL-ice I) and BL-VHDI also can be observed via compressing confined in width of 8 Å at 250 K.[21]

liquid−solid phase transitions, the elementary unit in the corresponding solid phase is different from each other. The ubiquitous Oswald staging phenomenon in these low-dimensional solid−liquid−solid phase transitions implies that from the perspective of geometric structures, the direct transformation among solids with different elementary units cannot be realized in 2D water/ice. The intermediate liquid (disordered) state seems necessary because the hydrogen-bonding network must be disrupted first to reconstruct a new hydrogen-bonding network in the course of solid−solid transformation among bilayer ices.

CONCLUSIONS

Based on extensive MD simulations, structural properties of BHI-AB and related phase behavior are investigated. BHI-AB can be derived by slowly reducing the nanoslit width, with BHI-AA as the initial structure in the nanoslit. It also can transform to BL-VHDI by the compression effect of lateral pressure. In both courses of phase transitions, a solid−liquid−solid phase transition behavior (or Oswald staging) can arise. The simulated TEM image of BHI-AB resembles, to some extent, that of the bilayer squarelike ice taken in the experiment. The realistic structure of BHI-AB, however, consists of two hexagonal monolayers, each with elongated hexagonal rings, and the hexagonal rings being slightly distorted with interior angle about 107 and 146°. The obtained T−h phase diagram exhibits a solid−liquid−solid triple point, where the second solid phase is the well-known bilayer hexagonal ice (i.e., the bilayer ice I) with an AA-stacking order (or the "Nebraska ice"). Such a solid−liquid−solid triple point exhibits some resemblance to that shown in the pressure−temperature phase diagram for bulk ice I−water−ice III phases. The new insights obtained from this systematic study of bilayer ices can be useful for understanding many intriguing phase behaviors of 2D water/ice.

COMPUTATIONAL DETAILS

MD Simulations. We carried out a series of classical MD simulations of water confined between two smooth hydrophobic surfaces in a wide range of slit width (separation of two surface, h = 7.6−8.5 Å) to explore the freezing of bilayer liquid water to bilayer ice. The temperature is lowered with an interval of 10 K. The simulation system consists of 512 water molecules. The water molecules interact with each other via the TIP4P/2005 pair potential[53] and with the smooth hydrophobic surfaces via the 9-3 Lennard−Jones (LJ) potential with LJ parameters of σ_{o-wl} = 0.25 nm and ε_{o-wl} = 1.25 kJ/mol, which is commonly used[9,22,54−57] to represent the effective interactions of water molecules with paraffin surfaces.[57] All simulations were performed in the isothermal/isolateral-pressure (NP_LT) ensemble with periodic boundary conditions in the lateral (x and y) directions, where P_L is the lateral pressure set at 450 MPa. Temperature (T) and the lateral pressure were controlled by the Nosé−Hoover thermostat[58,59] and Parrinello−Rahman barostat,[60] respectively. A cutoff of 1.0 nm was adopted for the LJ pair interactions, and the long-range electrostatic interactions were treated by the slab-adapted Ewald sum method.[61] Depending on the given h and T, an equilibration run was performed for 10 ns and in some cases up to 400 ns, with the time step of 2 fs.

To determine the location of phase boundaries in the h−T phase diagram, the transition temperatures are obtained based on the two-phase coexistence MD simulations,[9,62] which are carried out for the BHI-AA/liquid and BHI-AB/liquid in NP_LT ensemble. The simulations with a mixed system consists of half liquid and half solid (i.e., consist of 1024 water molecules) are carried out at pressure of 450 MPa. Depending on the given h and T, each equilibration run was performed for 40 ns. Furthermore, we performed a series of MD simulations to explore the transition from the bilayer hexagonal ice with an AA-stacking (BHI-AA) to the bilayer hexagonal ice with an AB-stacking (BHI-AB), with the BHI-AA as the initial structure, with gradually decreasing h value, from 8.4 to 7.7 Å. Then, we reduced the value of h with a step of 0.1 Å. Each equilibration run was performed for 100 ns. Again, the simulations were also carried out in the NP_LT ensemble, where the temperature was controlled at 210 K and pressure was at 450 MPa. Lastly, NP_LT MD simulations were performed to explore the compression effect of the lateral pressure on BHI-AB with h = 7.7 Å. The pressures were set as 1, 10, 100 bar, and 0.1−1.5 GPa with an interval of 0.1 GPa. For every pressure, the system fixed the temperature of 210 K. Depending on the given P_L and T, each equilibration run was performed for 40 ns.

In this work, the defect-free structures of BHI-AA and BHI-AB are obtained by cooling and heating the system repeatedly.

DOI: 10.1021/acs.jpcc.8b00195
J. Phys. Chem. C 2018, 122, 6704−6712

Specifically, to obtain a defect-free BHI-AB, we adjust the temperature with three steps: we decrease the temperature from 230 to 200 K, then increase it to 240 K, and lastly decrease it to 210 K. To obtain a defect-free BHI-AA, we decrease the temperature from 230 to 200 K at first and then increase it to 210 K. The temperature interval for all the simulations is 10 K, and each simulation lasts at least 200 ns.

DFT Calculations of Energies and Dynamic Stability. The energies and dynamic stabilities of BHI-AA and BHI-AB are investigated by using density functional theory (DFT) method with the CASTEP[42] program implemented in the Materials Studio 7.0 package. The plane wave basis set with an energy cutoff of 750 eV is employed together with norm-conserving pseudopotentials. The 5 × 7 × 5 Monkhorst–Pack[63] *k*-point grids are used for BHI-AA and BHI-AB structures with eight water molecules in each unit cell. The optimized structures of BHI-AA and BHI-AB are based on the PBE[43] exchange-correlation functional. To confirm their dynamic stability, the phonon dispersion is computed by using the density functional perturbation theory (DFPT)[44] as implemented in CASTEP.

Simulation of TEM Images. The simulated images (see Figures 4 and S4) were obtained in the following steps. First, the structural data of both crystals were obtained from the optimized structures of BHI-AA and BHI-AB by DFT. After that, the TEM images for both bilayer ice were simulated using QSTEM software[46] and the parameters corresponded to the experimental conditions[15] (accelerating voltage and spherical aberration coefficient).

■ ASSOCIATED CONTENT

Supporting Information

The Supporting Information is available free of charge on the ACS Publications website at DOI: 10.1021/acs.jpcc.8b00195.

A defect-free structure of BHI-AB and time-averaging structure in all of the MD snapshots within the last sampling time of 40 ns of MD simulation; density profile of BHI-AB in the *z*-direction, at T = 210 K; optimized structures of BHI-AB and BHI-AA based on the PBE-D exchange-correlation functional; simulated TEM image of BHI-AB based on a large-scale system; inherent structures of BL-VHDI phase formed in nanoslits (Figures S1–S5) (PDF)

Trajectories of the liquid–solid phase transition and the solid–liquid–solid phase transition for BHI-AB (AVI) (AVI)

■ AUTHOR INFORMATION

Corresponding Authors

*E-mail: yuanlf@ustc.edu.cn. Tel: 86-0551-63600994 (L.-F.Y.).
*E-mail: wuha@ustc.edu.cn. Tel: 86-0551-63601245 (H.A.W.).
*E-mail: xzeng1@unl.edu. Tel: 402-472-9894 (X.C.Z.).

ORCID

Jinlong Yang: 0000-0002-5651-5340
Xiao Cheng Zeng: 0000-0003-4672-8585

Notes

The authors declare no competing financial interest.

■ ACKNOWLEDGMENTS

This work was supported by grants from the National Natural Science Foundation of China (21503205 and 11574282), Anhui Provincial Natural Science Foundation (1608085QB30), Zhejiang Provincial Natural Science Foundation of China (LY18B030003), and US NSF CHE-1665324, and by the University of Nebraska Holland Computing Center. H.A.W. and Y.B.Z. were supported by the Strategic Priority Research Program of the Chinese Academy of Sciences (XDB22040402), the National Natural Science Foundation of China (11525211), and the National Postdoctoral Program for Innovative Talents (BX201700225).

■ REFERENCES

(1) Ball, P. *Life's Matrix: a Biography of Water*; University of California Press: Berkeley, CA, 2001.
(2) Mishima, O.; Stanley, H. E. The relationship between liquid, supercooled and glassy water. *Nature* **1998**, *396*, 329–335.
(3) Huang, Y.; Zhu, C.; Wang, L.; Cao, X.; Su, Y.; Jiang, X.; Meng, S.; Zhao, J.; Zeng, X. C. A new phase diagram of water under negative pressure: The rise of the lowest-density clathrate s-III. *Sci. Adv.* **2016**, *2*, No. e1501010.
(4) Koga, K.; Gao, G.; Tanaka, H.; Zeng, X. C. Formation of ordered ice nanotubes inside carbon nanotubes. *Nature* **2001**, *412*, 802–805.
(5) Maniwa, Y.; Kataura, H.; Abe, M.; Udaka, A.; Suzuki, S.; Achiba, Y.; Kira, H.; Matsuda, K.; Kadowaki, H.; Okabe, Y. Ordered water inside carbon nanotubes: formation of pentagonal to octagonal ice-nanotubes. *Chem. Phys. Lett.* **2005**, *401*, 534–538.
(6) Maniwa, Y.; Kataura, H.; Abe, M.; Suzuki, S.; Achiba, Y.; Kira, H.; Matsuda, K. Phase Transition in Confined Water Inside Carbon Nanotubes. *J. Phys. Soc. Jpn.* **2002**, *71*, 2863–2866.
(7) Byl, O.; Liu, J. C.; Wang, Y.; Yim, W. L.; Johnson, J. K.; Yates, J. T., Jr. Unusual hydrogen bonding in water-filled carbon nanotubes. *J. Am. Chem. Soc.* **2006**, *128*, 12090–12097.
(8) Bai, J.; Wang, J.; Zeng, X. C. Multiwalled ice helixes and ice nanotubes. *Proc. Natl. Acad. Sci. U.S.A.* **2006**, *103*, 19664–19667.
(9) Bai, J.; Angell, C. A.; Zeng, X. C. Guest-free monolayer clathrate and its coexistence with two-dimensional high-density ice. *Proc. Natl. Acad. Sci. U.S.A.* **2010**, *107*, 5718–5722.
(10) Zhao, W.-H.; Bai, J.; Yuan, L.-F.; Yang, J.; Zeng, X. C. Ferroelectric hexagonal and rhombic monolayer ice phases. *Chem. Sci.* **2014**, *5*, 1757–1764.
(11) Zangi, R.; Mark, A. E. Monolayer ice. *Phys. Rev. Lett.* **2003**, *91*, No. 025502.
(12) Zhu, Y.; Wang, F.; Wu, H. Superheating of monolayer ice in graphene nanocapillaries. *J. Chem. Phys.* **2017**, *146*, No. 134703.
(13) Johnston, J. C.; Kastelowitz, N.; Molinero, V. Liquid to quasicrystal transition in bilayer water. *J. Chem. Phys.* **2010**, *133*, No. 154516.
(14) Zangi, R.; Mark, A. E. Bilayer ice and alternate liquid phases of confined water. *J. Chem. Phys.* **2003**, *119*, 1694–1700.
(15) Algara-Siller, G.; Lehtinen, O.; Wang, F. C.; Nair, R. R.; Kaiser, U.; Wu, H. A.; Geim, A. K.; Grigorieva, I. V. Square ice in graphene nanocapillaries. *Nature* **2015**, *519*, 443–445.
(16) Zhu, Y.; Wang, F.; Bai, J.; Zeng, X. C.; Wu, H. Compression limit of two-dimensional water constrained in graphene nanocapillaries. *ACS Nano* **2015**, *9*, 12197–12204.
(17) Kaneko, T.; Bai, J.; Yasuoka, K.; Mitsutake, A.; Zeng, X. C. Liquid-solid and solid-solid phase transition of monolayer water: High-density rhombic monolayer ice. *J. Chem. Phys.* **2014**, *140*, No. 184507.
(18) Kwac, K.; Kim, I.; Pascal, T. A.; Goddard, W. K.; Park, H. G.; Jung, Y. Multilayer Two-Dimensional Water Structure Confined in MoS2. *J. Phys. Chem. C* **2017**, *121*, 16021–16028.
(19) Zhao, W.-H.; Bai, J.; Wang, L.; Yuan, L.-F.; Yang, J.; Francisco, J. S.; Zeng, X. C. Formation of bilayer clathrate hydrates. *J. Mater. Chem. A* **2015**, *3*, 5547–5555.
(20) Zhao, W.-H.; Wang, L.; Bai, J.; Yuan, L.-F.; Yang, J.; Zeng, X. C. Highly confined water: two-dimensional ice, amorphous ice, and clathrate hydrates. *Acc. Chem. Res.* **2014**, *47*, 2505–2513.

DOI: 10.1021/acs.jpcc.8b00195
J. Phys. Chem. C 2018, 122, 6704–6712

(21) Bai, J.; Zeng, X. C. Polymorphism and polyamorphism in bilayer water confined to slit nanopore under high pressure. *Proc. Natl. Acad. Sci. U.S.A.* **2012**, *109*, 21240−21245.
(22) Koga, K.; Tanaka, H. Phase diagram of water between hydrophobic surfaces. *J. Chem. Phys.* **2005**, *122*, No. 104711.
(23) Zangi, R. Water confined to a slab geometry: a review of recent computer simulation studies. *J. Phys.: Condens. Matter* **2004**, *16*, S5371−S5388.
(24) Zhu, W.; Zhao, W.-H.; Wang, L.; Yin, D.; Jia, M.; Yang, J.; Zeng, X. C.; Yuan, L.-F. Two-dimensional interlocked pentagonal bilayer ice: how do water molecules form a hydrogen bonding network? *Phys. Chem. Chem. Phys.* **2016**, *18*, 14216−14221.
(25) Chen, J.; Schusteritsch, G.; Pickard, C. J.; Salzmann, C. G.; Michaelides, A. Double-layer ice from first principles. *Phys. Rev. B* **2017**, *95*, No. 094121.
(26) Corsetti, F.; Zubeltzu, J.; Artacho, E. Enhanced configurational entropy in high-density nanoconfined bilayer ice. *Phys. Rev. Lett.* **2016**, *116*, No. 085901.
(27) Koga, K.; Tanaka, H.; Zeng, X. First-order transition in confined water between high-density liquid and low-density amorphous phases. *Nature* **2000**, *408*, 564−567.
(28) Jinesh, K. B.; Frenken, J. W. M. Experimental evidence for ice formation at room temperature. *Phys. Rev. Lett.* **2008**, *101*, No. 036101.
(29) Kimmel, G. A.; Matthiesen, J.; Baer, M.; Mundy, C. J.; Petrik, N. G.; Smith, R. S.; Dohnálek, Z.; Kay, B. D. No confinement needed: Observation of a metastable hydrophobic wetting two-layer ice on graphene. *J. Am. Chem. Soc.* **2009**, *131*, 12838−12844.
(30) Bampoulis, P.; Teernstra, V. J.; Lohse, D.; Zandvliet, H. J.; Poelsema, B. Hydrophobic ice confined between graphene and MoS_2. *J. Phys. Chem. C* **2016**, *120*, 27079−27084.
(31) Corsetti, F.; Matthews, P.; Artacho, E. Structural and configurational properties of nanoconfined monolayer ice from first principles. *Sci. Rep.* **2016**, *6*, No. 18651.
(32) Chen, J.; Schusteritsch, G.; Pickard, C. J.; Salzmann, C. G.; Michaelides, A. Two dimensional ice from first principles: Structures and phase transitions. *Phys. Rev. Lett.* **2016**, *116*, No. 025501.
(33) Walet, N. R. *Water Confined between Graphene Layers: The Case for a Square Ice*. 2017, arXiv:1702.00963. arXiv.org e-Print archive.
(34) Roman, T.; Groß, A. Polymorphism of water in two dimensions. *J. Phys. Chem. C* **2016**, *120*, 13649−13655.
(35) Mario, M. S. F.; Neek-Amal, M.; Peeters, F. AA-stacked bilayer square ice between graphene layers. *Phys. Rev. B* **2015**, *92*, No. 245428.
(36) Satarifard, V.; Mousaei, M.; Hadadi, F.; Dix, J.; Fernandez, M. S.; Carbone, P.; Beheshtian, J.; Peeters, F. M.; Neek-Amal, M. Reversible structural transition in nanoconfined ice. *Phys. Rev. B* **2017**, *95*, No. 064105.
(37) Koga, K.; Zeng, X. C.; Tanaka, H. Freezing of confined water: A bilayer ice phase in hydrophobic nanopores. *Phys. Rev. Lett.* **1997**, *79*, 5262.
(38) Jia, M.; Zhao, W.-h.; Yuan, L.-f. New Hexagonal-rhombic Trilayer Ice Structure Confined between Hydrophobic Plates. *Chin. J. Chem. Phys.* **2014**, *27*, 15−19.
(39) Zhu, Y.; Wang, F.; Wu, H. Buckling failure of square ice-nanotube arrays constrained in graphene nanocapillaries. *J. Chem. Phys.* **2016**, *145*, No. 054704.
(40) Rao, C. Theory of Hydrogen Bonding in Water. In *The Physics and Physical Chemistry of Water*; Springer, 1972; pp 93−114.
(41) Pauling, L. The structure and entropy of ice and of other crystals with some randomness of atomic arrangement. *J. Am. Chem. Soc.* **1935**, *57*, 2680−2684.
(42) Clark, S. J.; Segall, M. D.; Pickard, C. J.; Hasnip, P. J.; Probert, M. J.; Refson, K.; Payne, M. C. First principles methods using CASTEP. *Z. Kristallogr.* **2005**, *220*, 567−570.
(43) Perdew, J. P.; Burke, K.; Ernzerhof, M. Generalized gradient approximation made simple. *Phys. Rev. Lett.* **1996**, *77*, 3865.
(44) Refson, K.; Tulip, P. R.; Clark, S. J. Variational density-functional perturbation theory for dielectrics and lattice dynamics. *Phys. Rev. B* **2006**, *73*, No. 155114.
(45) Grimme, S. Semiempirical GGA-type density functional constructed with a long-range dispersion correction. *J. Comput. Chem.* **2006**, *27*, 1787−1799.
(46) Koch, C. T. *Determination of Core Structure Periodicity and Point Defect Density along Dislocations*. Ph.D. Thesis, Arizona State University, 2002.
(47) Kobayashi, K.; Koshino, M.; Suenaga, K. Atomically Resolved Images of I(h) Ice Single Crystals in the Solid Phase. *Phys. Rev. Lett.* **2011**, *106*, No. 206101.
(48) Kastelowitz, N.; Johnston, J. C.; Molinero, V. The anomalously high melting temperature of bilayer ice. *J. Chem. Phys.* **2010**, *132*, No. 124511.
(49) Han, S.; Choi, M. Y.; Kumar, P.; Stanley, H. E. Phase transitions in confined water nanofilms. *Nat. Phys.* **2010**, *6*, 685−689.
(50) Radha, B.; Esfandiar, A.; Wang, F. C.; Rooney, A. P.; Gopinadhan, K.; Keerthi, A.; Mishchenko, A.; Janardanan, A.; Blake, P.; Fumagalli, L.; Lozada-Hidalgo, M.; Garaj, S.; Haigh, S. J.; Grigorieva, I. V.; Wu, H. A.; Geim, A. K. Molecular transport through capillaries made with atomic-scale precision. *Nature* **2016**, *538*, 222−225.
(51) Takaiwa, D.; Hatano, I.; Koga, K.; Tanaka, H. Phase diagram of water in carbon nanotubes. *Proc. Natl. Acad. Sci. U.S.A.* **2008**, *105*, 39−43.
(52) Zhu, Y.; Wang, F.; Bai, J.; Zeng, X. C.; Wu, H. Formation of Trilayer Ices in Graphene Nanocapillaries under High Lateral Pressure. *J. Phys. Chem. C* **2016**, *120*, 8109−8115.
(53) Abascal, J. L.; Vega, C. A general purpose model for the condensed phases of water: TIP4P/2005. *J. Chem. Phys.* **2005**, *123*, No. 234505.
(54) Lee, S. H.; Rossky, P. J. A comparison of the structure and dynamics of liquid water at hydrophobic and hydrophilic surfaces—a molecular dynamics simulation study. *J. Chem. Phys.* **1994**, *100*, 3334−3345.
(55) Han, S.; Kumar, P.; Stanley, H. E. Hydrogen-bond dynamics of water in a quasi-two-dimensional hydrophobic nanopore slit. *Phys. Rev. E* **2009**, *79*, No. 041202.
(56) Lee, C. Y.; McCammon, J. A.; Rossky, P. J. The structure of liquid water at an extended hydrophobic surface. *J. Chem. Phys.* **1984**, *80*, 4448−4455.
(57) Kumar, P.; Buldyrev, S. V.; Starr, F. W.; Giovambattista, N.; Stanley, H. E. Thermodynamics, structure, and dynamics of water confined between hydrophobic plates. *Phys. Rev. E* **2005**, *72*, No. 051503.
(58) Nosé, S.; Klein, M. Constant pressure molecular dynamics for molecular systems. *Mol. Phys.* **1983**, *50*, 1055−1076.
(59) Hoover, W. G. Canonical dynamics: equilibrium phase-space distributions. *Phys. Rev. A* **1985**, *31*, 1695.
(60) Parrinello, M.; Rahman, A. Polymorphic transitions in single crystals: A new molecular dynamics method. *J. Appl. Phys.* **1981**, *52*, 7182−7190.
(61) Yeh, I.-C.; Berkowitz, M. L. Ewald summation for systems with slab geometry. *J. Chem. Phys.* **1999**, *111*, 3155−3162.
(62) Wang, J.; Yoo, S.; Bai, J.; Morris, J. R.; Zeng, X. C. Melting temperature of ice Ih calculated from coexisting solid-liquid phases. *J. Chem. Phys.* **2005**, *123*, No. 036101.
(63) Monkhorst, H. J.; Pack, J. D. Special points for Brillouin-zone integrations. *Phys. Rev. B* **1976**, *13*, 5188−5192.

DOI: 10.1021/acs.jpcc.8b00195
J. Phys. Chem. C 2018, 122, 6704−6712